Volumetric measurement of a Newtonian fluid flow through three-dimensional porous media using Lagrangian Particle Tracking (Shake-the-Box) technique

Maryam Bagheri [a], Parisa Mirbod [a,1]

[a] *Department of Mechanical and Industrial Engineer, University of Illinois at Chicago, Chicago, IL, 60607*

Abstract

This work experimentally investigates the pressure-driven flow of a pure Newtonian fluid through three-dimensional (3D) porous media models. The porous media model consists of square arrays of rods which also could be interpreted as a periodic tandem rod arrangement. We employed a time-resolved three-dimensional Particle Tracking Velocimetry (3D Shake-the-Box) technique for a range of the Reynolds numbers $111 \leq Re \leq 890$ to observe the flow structures and vortex formation between the rods in porous media structures with different porosities of $\varepsilon = 0.7, 0.8$, and 0.9 which corresponds to the spacing ratio of $\frac{L}{D} = 1.75,\ 2,$ and 3, where L is the distance between the centers of the rods and D is the diameter for the rods. For all the examined cases, we further analyzed the effect of the Reynolds number and the spacing ratio on the instantaneous and averaged patterns of velocity, vorticity, and the other flow parameters after obtaining the two-dimensional velocity fields using the bin-averaging method. We observed both symmetrical and asymmetrical patterns of structure of and recirculation regions between the rods depending on the Reynolds number and spacing ratio. Increasing the Reynolds number reduced the symmetrical patterns of flow structures with respect to the centerline of the gap region while the spacing ratio was randomly affecting the symmetry degree. Vortex shedding was considerable for the two examined high Reynolds numbers of *Re*= 444, and *Re*=890 behind the upstream rod as

[1] Email Address for Correspondence: pmirbod@uic.edu

the porosity increased. The backward movement of the reattachment point has been observed by increasing the Reynolds number.

I. Introduction

In the last few decades, there has been extensive research on laminar and turbulent channel flows around wall-attached obstacles, including two rods in tandem with various rods spacing. The complex flow structures in the wake of multiple circular rods in side-by-side configuration have attracted considerable attention due to their fundamental physics and relevance to offshore and ocean engineering applications such as risers, mooring lines, and pipelines. In the earlier studies, Zdravkovich[1] discussed the flow interference between two rods in tandem arrangement and categorized the flow around two tandem rods into three different flow regimes based on the different spacing ratios ($\frac{L}{D} < 6$) followed by the classification of flow regimes in the function of the Reynolds numbers in earlier studies by Igarashi [2, 3]. Sumner, Price *et al.* [4] studied the flow field for circular rods of equal diameter arranged in tandem using flow visualization and two-dimensional (2D) particle image velocimetry (PIV) over a longitudinal pitch ratio range of $\frac{L}{D} = 1 - 3, and\ Re = 1200 - 3800$. The gap between the rods resulted in a shear-layer-reattachment flow pattern under steady conditions. Lin *et al.*[5] utilized high-image-density particle image velocimetry to characterize the instantaneous and averaged patterns of velocity, vorticity, and Reynolds stress due to flow past two rods in a tandem arrangement at *Re*=10,000. They discussed the formation of Karman-like vortices between the rods when the gap region is sufficiently large. Xu and Zhou [6] investigated the vortex-shedding frequencies of the tandem rods using two hot wires placed behind each rod for a wide range of the Reynolds numbers ($800 \leq Re \leq 42000$) and spacing ratios ($1 \leq \frac{L}{D} \leq 15$), while Zhou and Yiu [7] studied flow structure in the wake of two tandem rods using hot wire velocimetry conducted at $\frac{L}{D} = 10, 20, 30$, and $Re = 7000$. Two different flow structures in the reattachment regime were identified. The shear layer reattachment occurred at the rear surface of the downstream rod for $2 \leq \frac{L}{D} \leq 3$, while it occurred at the leading surface of the downstream rod for $3 \leq \frac{L}{D} \leq 5$. Neuhart et *al.*[8] examined the unsteady wake interference between two tandem rods at $Re = 1.66 \times 10^5$ using PIV technique, and studied the effect of boundary layer tripping along the downstream rod for different spacing ratios. Their PIV data revealed the separated shear layers from the rods and the resulting unsteady interactions with the downstream rod surface. They also reported a rapid increase in pressure drag occurring near $\frac{L}{D} = 3$. Tsutsui[9] examined the fluctuation of the fluid forces acting on the tandem rods for $\frac{L}{D} = 1.2$ at ($3.8 \times 10^4 \leq Re \leq 1.3 \times 10^5$) in a wind tunnel via hot wire technique. They found that the separated shear layer from the first rod's upper and lower sides reattaches to the upper and lower sides of the second rod. Weinmann et al.[10] applied a numerical model, which combines the Reynolds-Averaged Navier-Stokes (RANS) and Large Eddy Simulations (LES), to simulate the flow around the two tandem rods at $Re = 1.66 \times 10^5$ for $\frac{L}{D} = 3.7$, and the computed surface pressure distributions were compared with the experimental data. They performed an assessment for the flow and noise prediction of a tandem rod configuration which showed a good agreement with the experimental results. Later, Gopalan and Jaiman[11] simulated the flow interference between rods based on the hybrid RANS and LES methods with non-linear eddy viscosity formulations at $Re = 1.66 \times 10^5$ for $\frac{L}{D} = 1.4, 3, 3.7$. The bi-stable wake between the rods and the drag inversion on the downstream rod was observed for $\frac{L}{D} = 3$. They also found that the bi-stable wake led to an increase in the turbulent kinetic energy in the gap between the rods. Following our prior works of understanding flows over and through porous structures with the broad applications of porous media structures in industrial and biomedical fields such as extrusion and thin lubricating film technologies, filtration processes, and even blood flows in micro vessels[12], we aimed to study the flow behavior in the gap region of two adjacent rods in a porous media made of square arrays of rods in the direction of flow as a new avenue of the study compared to the existing literature mentioned above. Specifically, we used micro-Particle tracking velocimetry Shake-the-Box (STB) technique which gives the capability to focus on two adjacent rods to further examine the flow between two rods. Particle tracking velocimetry using Shake-the-Box (STB) technique has been introduced and developed by Schanz *et al.*[13]. This novel dense Lagrangian particle tracking (LPT) technique (STB) provides temporally resolved (3D) data of the flow. The 3D STB, in principle, can be adapted to flows with much higher Reynolds numbers and flow conditions that currently are beyond to reach of numerical techniques. The employed measurement techniques are capable of very high dynamic temporal and spatial range, at least for one point statistics of the velocity vector data in small fields of view[14] or by multi-pulse STB[15, 16]. This technique has also been utilized by Schröder *et al.*[17] to experimentally investigate the flow separation and the development of related shear layers in a periodic hill water tunnel and provide reliable data for the validation process. They highlighted the possibility of achieving very high spatial resolution for the profiles of the bin-averaged velocity and Reynolds stress components. The advantages of using the combined data of both Lagrangian and Eulerian reference frames for investigating the dynamics of Lagrangian tracks for turbulence production have also been addressed through their work. This technique has also been used in a vertical water tunnel measurement facility by Tan et al.[18]. They demonstrated how this method is significantly reducing the processing time compared with Tomo-PIV at a similar particle image density.

To the best of our knowledge, however, all the flow behavior analysis for these systems have been performed using either numerical methods or the 2D flow visualization techniques via experiments. In addition, the majority of the existing literature has been attributed to the air cross flowing the rods to investigate the aerodynamic applications, particularly for supercritical high Reynolds numbers. For the first time, using the 3D Lagrangian particle tracking velocimetry technique (3D STB), we investigate the characteristics of the flow between rods in porous media models at relatively lower Reynolds numbers $111 \leq Re \leq 890$ due to the lack of experimental data on low Reynolds number flow regimes. Herein, we explore different porous media models with porosity of $\varepsilon = 0.7,\ 0.8,$ and 0.9 which corresponds to the spacing ratio of $\frac{L}{D} = 1.75, 2, 3$ where L is the distance between the center of the rods and D is the diameter for the rods. The flow structures, velocity trajectories, 2D velocity and, vorticity fields are also analyzed and discussed in detail. This paper is organized as follows. In Section II, we provide a description of the experimental setup and the procedures. In Section III, we analyze the results for the flow structure, velocity trajectories, 2D velocity, and vorticity fields at different Reynolds numbers, discuss their variation with respect to porosity or spacing ratios ($\frac{L}{D}$). Finally, concluding remarks are presented in Section IV.

II. Experimental Procedure:

A. Experimental Setup, PTV/Shake-the-Box system, and measurement Procedure

The flow channel for this test is constructed from high quality, clear, cast acrylic [19], as can be seen in Figures 1(a) and (b). The porous media model is constructed via a 3D printer (ProJet, University of Illinois at Chicago) using VisiJet Crystal. The porous media model consists of rods in a square array aligned perpendicular to the flow direction. The permeability was calculated using a series of equations proposed by Tamayol and Bahrami [20] for fibers in a square array. Table I reports the parameters used in this study (shown in Figures 1), including porosity (ε) of the porous region, rod diameter (D), spacing between the rods (S), the distance between the rod centers (L), and height of rods (h_p), the free flow gap in the channel ($h_{free\ flow}$), width of the channel (W), and the permeability (K) of the porous media. The reported parameters in the three rows of Table I, $\varepsilon = 0.7\ \left(\frac{L}{D} = 1.75\right)$, $\varepsilon = 0.8\ \left(\frac{L}{D} = 2\right)$, and $\varepsilon = 0.9\ (\frac{L}{D} = 3)$, correspond to the images in Figure 1 (d), (e), and (f), respectively. Since the height of the three different porous media that we used is h_p =3mm, and our cameras can capture the maximum volume thickness of 2 mm (in z direction), we attempted to place the volume measurement precisely in the middle of the height of the porous media. Thus, the measurement volume is between h= 0.5 mm and h= 2.5 mm, where h=0 represents the rod bottom surface (shown in FIG.1c). A peristaltic pump (MasterFlex L/S, Cole-Parmer) has been used in the flow loop with two pump heads (Easy Load II, ColeParmer). The pump heads feed into a Y fitting, which connects to a dampener (Masterflex Pulse dampener, Cole-Parmer). The combination of the Y fitting and the dampener helps reduce any pulsating from the pump, so the resulting flow is smooth and at a constant speed when it enters the flow channel. A reservoir fitted with two outlets and one inlet was set between the outlet of the flow channel and before the peristaltic pump, which closes the flow loop. For each experiment, the seeding particles in the fluid were mixed for 1 hr. on a magnetic mixer within the reservoir, and then was placed in an ultrasound vibrator (Cole-Parmer) in order to prevent any particle accumulation or clustering effects. Then, the fluid is placed into a vacuum chamber and subjected to a pressure of 0−30 inHg and kept for an additional one hour to remove any ambient air bubbles from the working fluid. It should be noted that once the pump was started, the flow ran for 30 min to stabilize through the flow loop and reach a steady-state condition before any data were collected.

Table I. Experimental parameters and physical properties of the examined porous media models demonstrated in Fig. 1.

	ε	*D (mm)*	*S (mm)*	*L (mm)*	h_p *(mm)*	$h_{free\,flow}$ *(mm)*	*W (mm)*	*K* (m^2)
FIG. 1(d)	0.7	2	1.5	3.5	3	4	25.4	1.12×10^{-3}
FIG. 2(e)	0.8	2	2	4				3.42×10^{-3}
FIG. 3(f)	0.9	1.5	3	4.5				7.93×10^{-3}

Flow-volume measurements were developed using a LaVision Flow Master particle tracking velocimetry (PTV/Shake-the-Box) system. This consisted of a 527 nm Nd-YLF (Photonics Industries, DM20-527) to illuminate the tracer particles that are seeded within the flow[21-23], as well as two high-speed complementary metal-oxide semiconductor (CMOS) cameras with a pixel field of view (FOV) and a full-scale resolution. All hardware timing and software were handled using the DaVis10.2.1 software package on the Intel (R) Xeon (R) CPU with 32.0 GB RAM and a 64-bit operating system. The (STB) system resulted in a maximum image size of 1200 x 1920 pixels which produced a field of view (FOV) that was approximately 8 mm × 6 mm at the least magnification of the microscope, which is marked as 1. This corresponds to a 2mm depth of measurement in volume. The physical FOV size has been reduced, allowing for larger data sets based on the experiments being conducted.

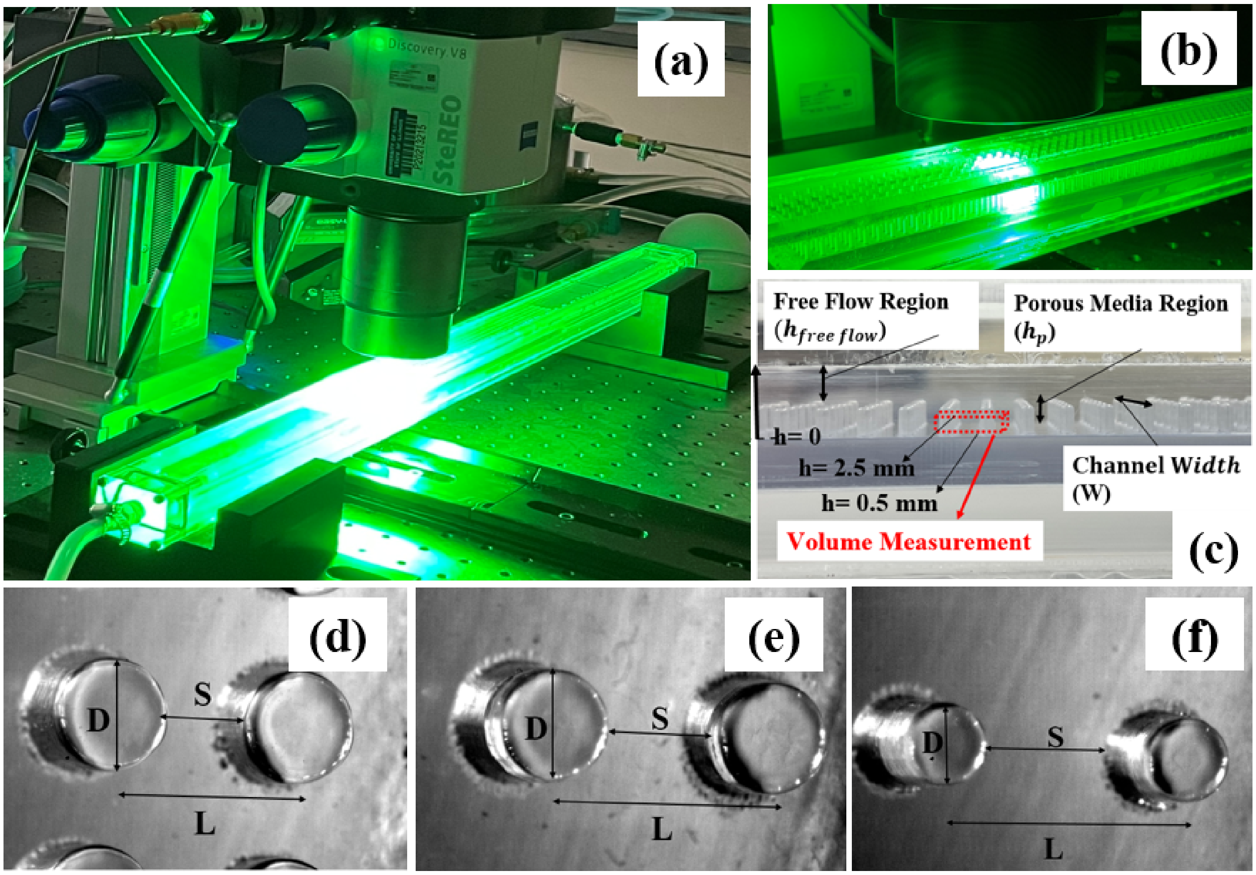

FIG. 4. a) A photo of the experimental setup and the STB measurement system, b) Illuminated volume for the measurement, c) geometrical parameters of the test section, and d, e, f) images taken with the same microscope in the STB system to show the geometrical parameters for different porous media used in this study for $\varepsilon = 0.7$ $\left(\frac{L}{D} = 1.75\right)$, $\varepsilon = 0.8$ $\left(\frac{L}{D} = 2\right)$, and $\varepsilon = 0.9$ $(\frac{L}{D} = 3)$, respectively.

B. Working fluid, seeding particles, and dimensionless parameters

The polymathic methacrylate (PMMA) with the mean diameter size of 3 μm and a standard deviation of 2 μm has been used as seeding particles in water. In order to reduce the effect of particle clustering, an ultrasound shaking machine (Cole-Parmer) was used to reach a uniformly distributed particle diameter range in the fluid. DI Water has a density of $\rho{\sim}1000\ \frac{kg}{m^3}$ and viscosity of $\mu{\sim}\ 0.001\ Pa.s$ and $\rho_p = 1180\ \frac{kg}{m^3}$ is the density of PMMA particles. Since there is a slight mismatch between the density of the PMMA particles and the solvent, the settling velocity $U_{settling} = \frac{g\ (\rho_p - \rho_f) d^2}{18\ \mu_f}$ was calculated to ensure that the particles remain suspended during testing.

This settling velocity mathematically considers the mismatch of the fluid densities along with the interaction of the particles as higher particles would travel down to the bottom wall [24]. The settling velocity of the PMMA particles was calculated as $2.45 \times 10^{-3}\ \frac{mm}{s}$, which is less than 0.004% of the average velocity within the channel, allowing this solution to be stable enough for the tests performed. Table II reports all the related dimensionless parameters for three different flow rates studied in this work. In the second column, we calculated the Reynolds number for the fluid based on the free flow height, $h_{free\ flow}$, as the characteristic length. U_{bulk} indicates the velocity calculated based on the flow rate running in each experiment and the cross-sectional area of the free flow region following our previous works [25, 26]. Third column reports the Reynolds number for fluid based on the rod diameter (*D*), as the characteristic scale [27-32]. The Forth column also represents, $Re_{seeding\ particles}$ which is the particle Reynolds number based on the averaged diameter of the seeding particles (d_p) that describes the motion of the fluid around the individual seeding particles [33]. This number was kept very small, which allowed for inertial effects on the particles to be neglected [34]. Therefore, the motion of the seeding particles was only dependent on the motion of the fluid. We have also reported the seeding particle's Stokes number as $St_{(seeding\ particles)}$. For all experiments performed in this study, the Stokes number was kept low, so the suspension particles did not have their own momentum within the flow [33]. It should be mentioned that the reported Reynolds number in the results and discussion section refers to the calculated Reynolds number in the second column of Table II.

Table II. Dimensionless flow parameters for three different flow rates studied in this work.

Nominal Flow Rate on the Pump (mL/min)	***Re** (free flow height)* $\frac{\rho U_{bulk}\, h_{free\,flow}}{\mu}$ $\varepsilon = 0.7$, $\varepsilon = 0.8$, $\varepsilon = 0.9$	***Re** (rod diameter)* $\frac{\rho U_{bulk}\, D}{\mu}$		$Re_{(seeding\ particles)}$ $\frac{2\rho(d_p)^3 U_{bulk}}{3\mu(h_{free\,flow})^2}$	***St** (seeding particles)* $\frac{\rho_p(d_p)^2 U_{bulk}}{18\mu}$
		$\varepsilon = 0.7$, $\varepsilon = 0.8$	$\varepsilon = 0.9$		
100	1.11×10^{2}	5.56×10^{1}	4.1×10^{2}	3.62×10^{-8}	1.14×10^{-5}
400	4.44×10^{2}	2.22×10^{2}	1.67×10^{2}	1.45×10^{-7}	4.55×10^{-5}
800	8.8×10^{2}	4.44×10^{2}	3.33×10^{2}	2.89×10^{-7}	9.10×10^{-5}

C. Velocity measurements using (PTV/Shake-the-Box) protocol

The Perspective calibration has been performed before conducting any volume self-calibration or optical transfer function (OTF) as a mandatory step for volumetric (PIV/PTV)[35]. We used the 300μm microplate from Lavision as the calibration target. A volume calibration is a camera calibration that maps the 3D components of the physical test section. To record several calibration views, the calibration plate is placed at three different positions in the measurement volume. An acrylic sheet with the same thickness as the channel was used in addition to a few drops of the working fluid in order to resemble the optical access of the test section. We recorded several calibration views in z=0 and then relocated the calibration plate upwards and downwards to cover the whole volume measurements (z=-1 mm to z=1 mm). In different environments, this substantially helped in finding the location of the volume measurement concerning for the light deviations. Image pre-processing is used to enhance the particle image quality and to remove background noise or artifacts. We then use the same image pre-processing to calculate the (OTF) and Shake-the-Box particle trajectory.

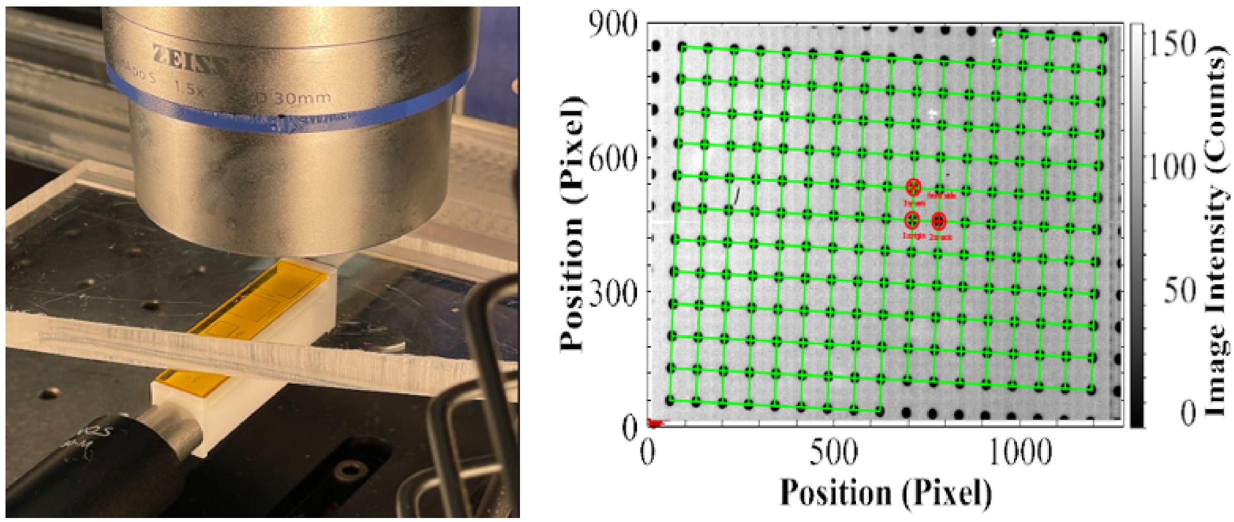

(a) (b)

FIG. 5. a) the physical demonstration of calibration (MP 300 μm used as the target) with a sheet of acrylic with the same thickness of the test section and the working fluid in between, and b) demonstrated calibration scales in Davis software.

A sample of raw particle images for three different porosities (reported in Table I) has been shown in Fig. 3. Pre-processed particle images have been used to do volume self-calibration. Volume self-calibration is a required step in the PTV procedure[36], which seeks to eliminate any remaining calibration inaccuracy after computing the disparity vectors. Volume self-calibration performs an iterative process until the remaining calibration inaccuracies fall below some threshold (0.1 voxel in this study) and the calibration does not improve any longer. Then, the average particle pattern on each camera for a certain sub-volume is produced. Later, these average particle patterns are used to fit the Optical transfer function (OTF). An elliptical Gaussian model is fitted for each sub-volume and each camera to represent the OTF.

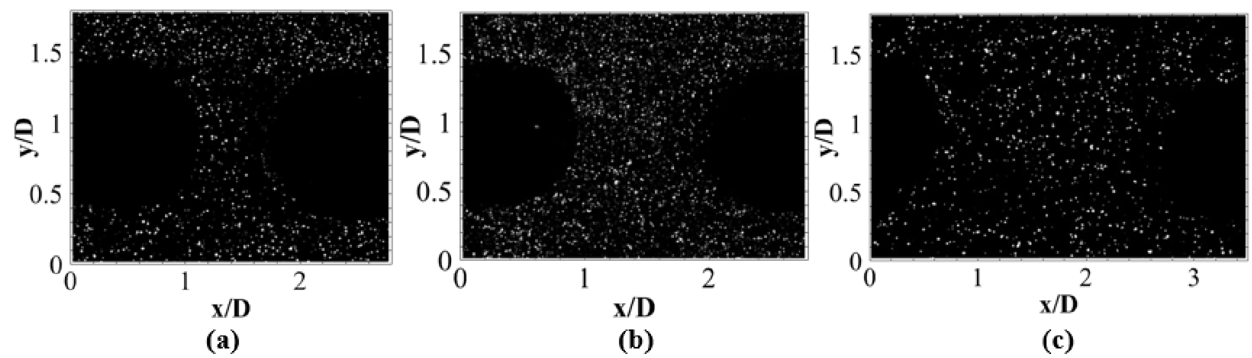

FIG. 3. Samples of raw particle images captured for characterizing the flow patterns between the two rods of porous media layer: a) $\varepsilon = 0.7$ $\left(\frac{L}{D} = 1.75\right)$, b) $\varepsilon = 0.8$ $\left(\frac{L}{D} = 2\right)$, and c) $= 0.9$ $(\frac{L}{D} = 3)$ at Re=111. The data represents the center plane in the volume measurement z=0.

III. Results and Discussion

To determine the data acquisition location for these experiments, we first ensured that the flow is fully developed over the porous media. Following our previous work [25], data were collected at various locations along the direction of the flow to determine which flow patterns remain constant downstream of the inlet. The analysis was performed at different examined Reynolds numbers in this study, but we report a sample of our results for Re=111 in Fig. 4. It should be noted that the proof of fully developed flow over porous media using 2D PIV measurement was previously reported in the study by Haffner and Mirbod[25], which demonstrated that the parabolic velocity profiles for the free flow region collapsed onto the theoretical profile[37 38], indicating that the flow at that point was fully developed. However, since the measurement field of view in this study is a volume that focuses on the area between the two rods in the porous region, different compared to our previous work (2D PIV analysis), we have then examined the fully developed flow in this specific region. To ensure no wall effects, we collected data from the center region of the channel through the width direction. Fig. 5 demonstrates the time-averaged streamline velocity profiles at Re =111 for different locations of $x = 430\ mm$, $x = 439\ mm$, and $x = 448\ mm$ obtained in the channel while x represents the distance from the inlet of the channel. As shown in Fig. 5, these profiles collapsed into one single curve, confirming the fully developed flow at these locations. The data reported in the following sections correspond to $x = 430\ mm$, which is the distance from the channel inlet. Furthermore, we initially acquired some preliminary data to ensure we were not overlooking the spanwise effect since we had square arrays of the rods both in the streamwise and spanwise directions. To visualize the flow at different arrays of the porous media, we moved our channel in the spanwise direction. As an example, for the case of $\varepsilon = 0.7$ ($\frac{L}{D} = 1.75$), we have 7 arrays in the spanwise direction, the data reported in our work is for the middle array which is the 4^{th} array from each channel wall. It was observed that It was observed that close-to-wall flow patterns were different from those away from the wall, which is due to near-wall effects in pressure-driven flow and no-slip boundary conditions at the walls[39-42]. The flow patterns were the same for the three arrays of rods in the middle (3^{rd}, 4^{th}, and 5^{th} arrays). As a result, we recorded the data for the array in the center of the channel (the fourth array of rods in this case).

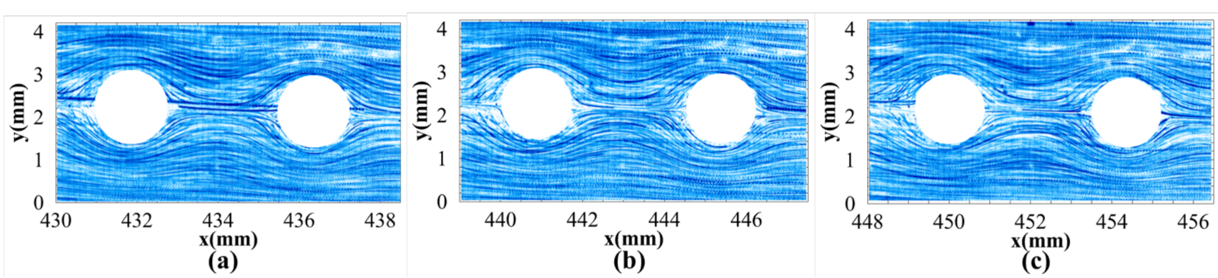

FIG 6. Time-averaged flow streak lines at different location of the channel: a) $x = 430\ mm$, b) $x = 439\ mm$, and c) $x = 448\ mm$. All the data corresponds to *Re*=111, and the porous layer with porosity of $\varepsilon = 0.9$ ($\frac{L}{D} = 3$). The data represents the center plane in the volume measurement z=0.

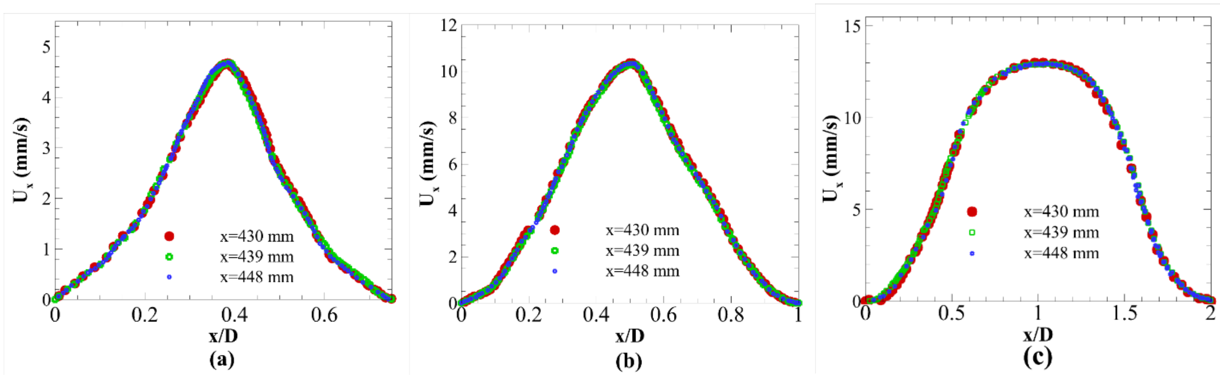

FIG 7. Time-averaged streamwise velocity profiles along the centerline in the gap region between the rods based on the spacing ratio of $\frac{L}{D}$ in a porous media model with porosity of a) $\varepsilon = 0.7$ $\left(\frac{L}{D} = 1.75\right)$, b) $\varepsilon = 0.8$ $\left(\frac{L}{D} = 2\right)$, and c) $= 0.9$ $(\frac{L}{D} = 3)$. The measurements correspond to different location of the channel $x = 430\ mm$, $x = 439\ mm$, $x = 448\ mm$ examined at *Re* =111.

In order to characterize different flow regimes and to examine the flow conditions between two rods, we plotted the averaged 2D streak lines of the seeding particles for different porosities (or various space ratios) by increasing the Reynolds numbers. Images were acquired at a range of 0.6 - 2.4 kHz based on the examined flow rate corresponding to a duration of 2.08 - 8.3 s (5000 images). To increase the frequency and have particle shift up to 10 pixels between any of the two image pairs, the measurement field of view was reduced for acquiring data at higher flow rates. Fig. 6 shows the time-averaged streak lines of the flow around the two rods, which involve symmetrical and asymmetrical patterns with respect to the centerline of the gap region. Fig. 6 (a, b, c) shows the streak lines for $\varepsilon = 0.7$ $(\frac{L}{D} = 1.75)$ at *Re* = 111, 444, 890. In general, the flow patterns in Fig 6 (a, d, g) indicate a uniform time-independent trend at *Re* =111, as it appears to be in the flow regime where the streamlines are parallel. Fig. 6 (a) exhibits a symmetrical pattern of the flow with respect to the centerline of the gap region between the upstream and downstream rods. As Reynolds number increase, Fig. 6 (b, c), two recirculation regions form in both the upper and lower portion of the gap. These recirculation regions start to become more well-defined and more prominent as the Reynolds number increases[43]. A similar pattern of streamline can be found in the flow measurement by Neuhart *et al.* [8] for $\frac{L}{D} = 1.435$ although at $Re = 1.66 \times 10^5$. This observation is slightly different for the porous layer with a porosity of $\varepsilon = 0.8$ ($\frac{L}{D} = 2$) shown in Fig. 6 (d, e, f). At *Re*= 111, the flow patterns are smooth between the rods, but with the flow rate increasing, the two recirculation regions appear considerably closer to the upstream rod, and it leads to the formation of a region free of vortices close to the downstream rod, which makes the flow moving in a positive direction. This degree of asymmetry has also been observed in the study by Lin *et al.* [5] for the cases of $\frac{L}{D} = 1.5$ and 2 while at $Re = 10^4$. It is also evident in Fig. 6 (f), that with increasing the Reynolds number to 890, the vortices grow noticeably for the one below the centerline of the region between the rods. Looking at the flow patterns for $\frac{L}{D} = 3$ and the porosity of $\varepsilon = 0.9$, the gap between the rods is sufficiently large that Karman-like vortices are generated in the region for higher flow rates with *Re*= 444, and *Re*= 890 Fig. 6 (h, i). This can be observed as a repeating pattern of swirling vortices caused by vortex shedding, which is responsible for the unsteady separation of flow between the rods, as reported by previous works [5, 44-46]. Also, as the spacing ratio increases from $\frac{L}{D} = 2$ in Fig. 6 (d, e, f) to $\frac{L}{D} = 3$ in Fig. 6 (g, h, i), the vortices become more non-uniform and chaotic.

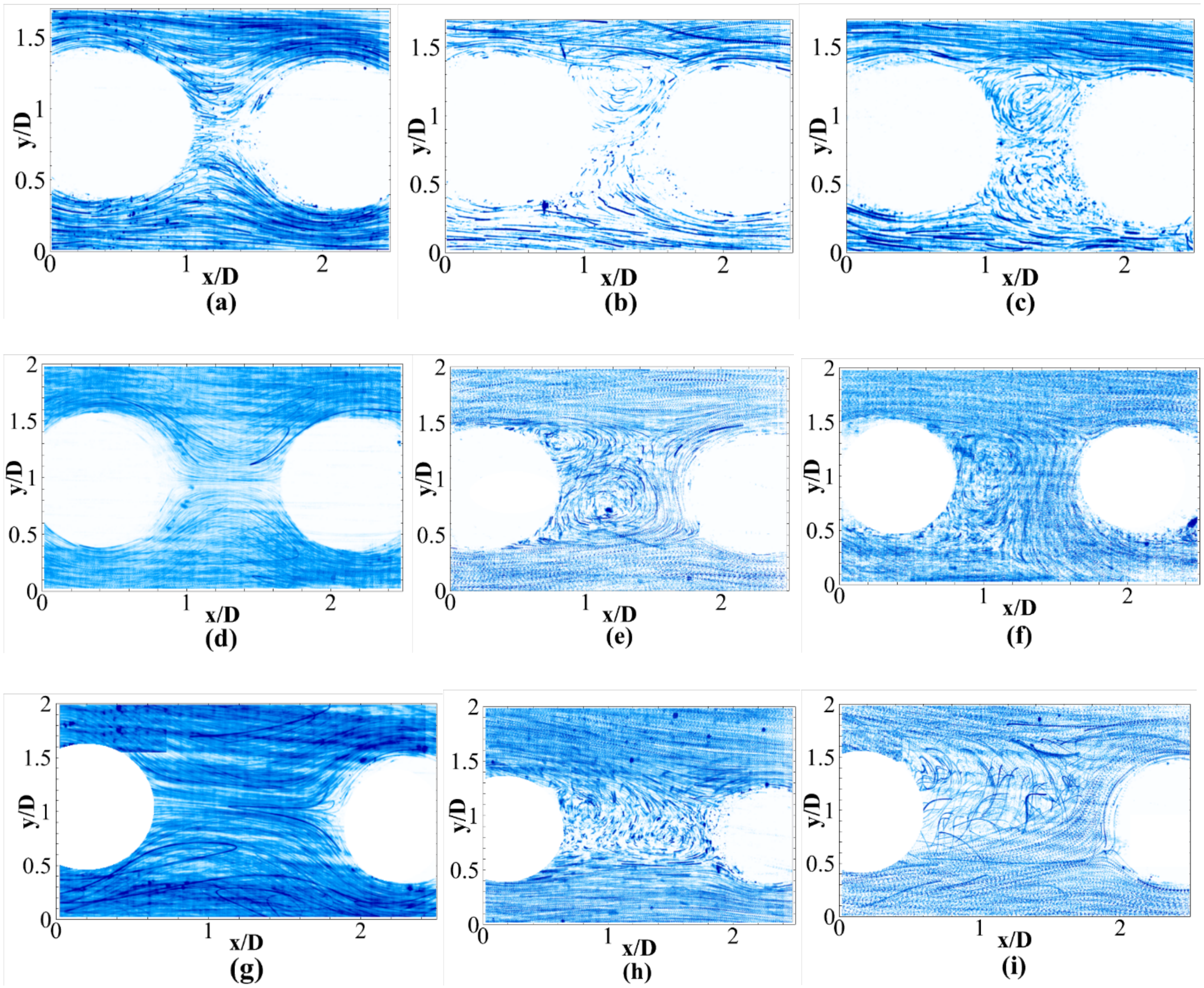

FIG. 8. Time-averaged streak lines for the flow around the rods: a) *Re*= 111, b) *Re*= 444, c) *Re*= 890 represent the patterns for $\varepsilon = 0.7$ ($\frac{L}{D} = 1.75$), d) *Re*= 111, e) *Re*= 444, f) *Re*= 890 represent the patterns for $\varepsilon = 0.8$ ($\frac{L}{D} = 2$), and g) *Re*= 111, h) *Re*= 444 , i) *Re*= 890 represent the patterns for $\varepsilon = 0.9$ ($\frac{L}{D} = 3$). The data represents the center plane the volume measurement z=0.

A Lagrangian particle tracking (LPT) method based on the Shake-The-Box (STB) algorithm ,introduced by Schanz *et al.*[13], was used to evaluate the volumetric flow dynamics. Fig. 7 shows the results for different Reynolds numbers within the reconstructed volume of around 10,000 particles which were instantaneously tracked over many time steps, and then the velocity was computed. In the z direction, the volume measurement ranges between z= -1 mm and z= 1mm, where z=0 is the center plane. Fig. 7(a, b, c) corresponds to $\varepsilon = 0.7$ ($\frac{L}{D} = 1.75$), Fig. 7 (d, e, f) corresponds to $\varepsilon = 0.8$ ($\frac{L}{D} = 2$), while Fig. 7(g, h, i) corresponds to $\varepsilon = 0.9$ and all the data obtained at Re = 111, 444, 890. Here, the trajectory and velocity of particles approaching in between the rods can be observed. It should be mentioned that the magnitude of velocity is calculated considering the three components (in the direction of x, y, and z) of the velocity vectors $|\mathrm{V}| = \sqrt{{U_x}^2 + {U_y}^2 + {U_z}^2}$. Also, the velocity error was determined as $rms_V = \sqrt{\frac{1}{N}\sum_1^N(\vec{V}_R - \vec{V}_S)^2}$ where $\vec{V}_R$ and $\vec{V}_S$ are respectively reconstructed and reveal the original velocity for each particle, and N represents the number of images [13, 47]. The calculated error was not greater than 0.08 pixel/time-step in our experiment. As shown in Fig. 7, with increasing the Reynolds number, |V| is increased, and the maximum velocity of the tracked particles is observed at the free stream regions, which are not obstructed by the rods. In general, the velocity of tracked particles is being reduced between the rods. Particles deflected downward and moved into the vortices in between the rods at higher Reynolds numbers Re= 444, and 890. It should be noted that for $\varepsilon = 0.7$ ($\frac{L}{D} = 1.75$), the detected particles in the gap region are not considerable compared to $\varepsilon = 0.8$ ($\frac{L}{D} = 2$) and $\varepsilon = 0.9$ ($\frac{L}{D} = 3$) as the distance between the rods is smaller. Trajectories bent around the rods show the formation of vortices. Median filters are used to remove spurious tracks that do not fit the neighboring tracks. By making so, wrong tracks or ghost tracks can be removed [48, 49]. The specified length of the particle tracks was adjusted between 4-10 time steps, and the range for velocity limits was adjusted in a way that particle tracks are not missing in any part of the measurement volume. Also, in order to enforce the temporal matching of true matching particles and to exclude unlikely tracks, the allowed acceleration was limited to 1 voxel[13].

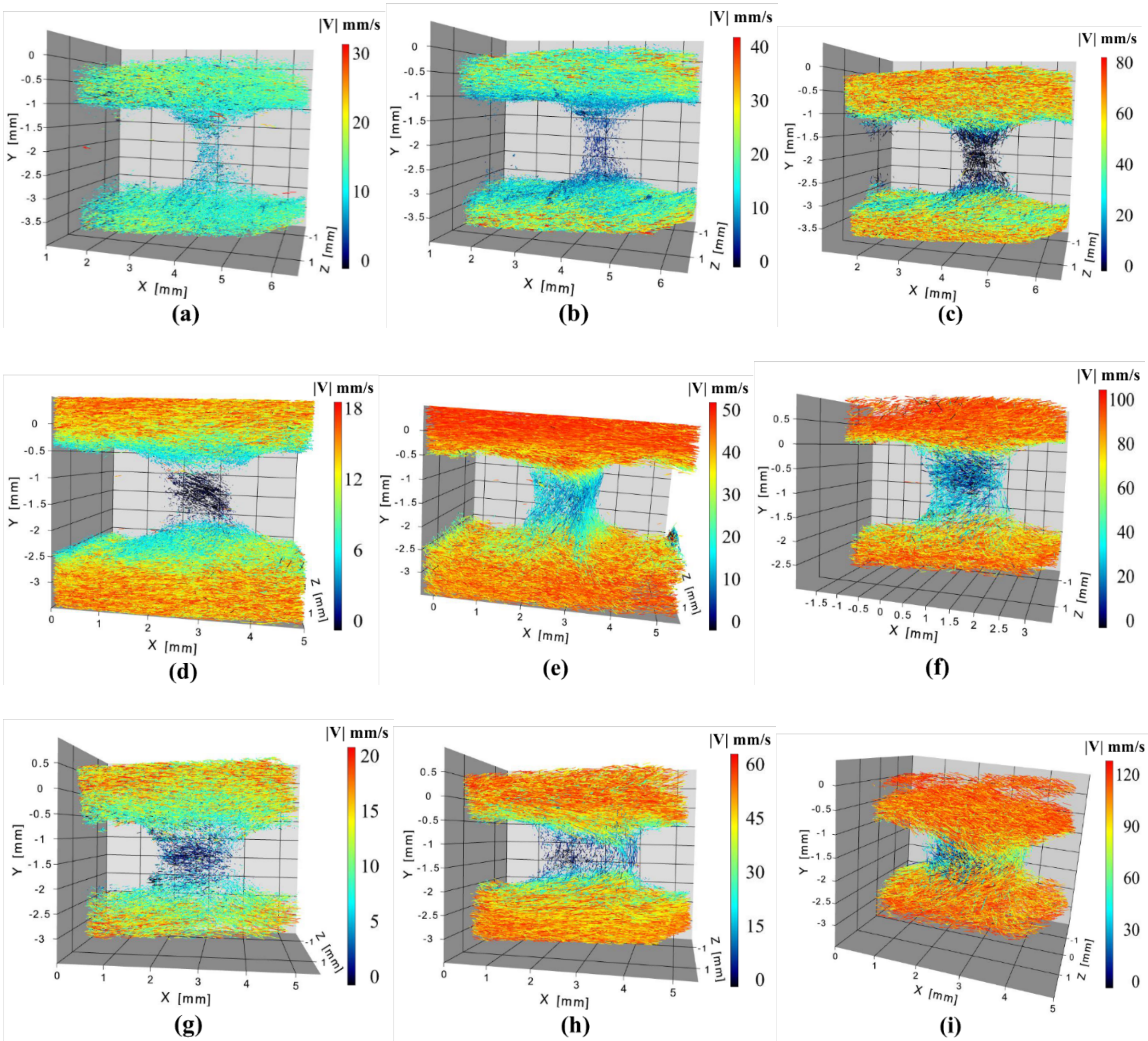

FIG. 9. Velocity magnitude results of particles trajectories obtained by 3D volumetric measurement: a) *Re*= 111, b) *Re*= 444, c) *Re*= 890 represent the patterns for $\varepsilon = 0.7$ ($\frac{L}{D} = 1.75$), d) *Re*= 111, e) *Re*= 444, f) *Re*= 890 represent the patterns for $\varepsilon = 0.8$ ($\frac{L}{D} = 2$), and g) *Re*= 111, h) *Re*= 444 , i) *Re*= 890 represent the patterns for $\varepsilon = 0.9$ ($\frac{L}{D} = 3$).

We then utilized the statistical method of "bin-averaging" as a post-processing step to convert the available high spatial resolution velocity or acceleration from particle tracking Shake-the-Box to a regular grid. This method has also been used in a recent work by Schröder *et al.* [50] where they investigated the flow around a cube. The complete data set of about 5000 time steps of the tracking results are used to create a dense grid of 100 × 100 bins with an individual cubic bin size of 0.0052 mm^3 with 75% overlap. The relative uncertainty of the averaged velocity was computed as $V_{unc} = \frac{\sigma}{\sqrt{N}}$ where (σ) is calculated from the standard deviation (σ) of all velocity vectors within the bin and *(N)* is the number of contributing images. The associated error for these experiments was not greater than 0.67% of the maximum velocity. Then, 100 segments of velocity fields were produced in the (x-y) plane throughout the depth of the measurement. Based on reported literature and also experimentally measured (2D-PIV) in our previous work [25], the magnitude of velocity shows an exponential curve in the porous region. We also observed that the magnitude of the streamwise velocity is slightly varying in the z direction (in the direction of the height) in the extracted planes from the bin-averaging method. A result of the converged mean flow field (averaged from the segmented planes through 2 mm depth of volume measurement) color-coded by the magnitude of velocity is given in Fig. 8. In general, velocity contours presented here demonstrate the dependence of the velocity magnitude between the rods on the spacing ratio and Reynolds number. As observed in figures 8 (a-i), velocity is decreased between the rods, and the formation of vortices becomes present by increasing the Reynolds number. Compared to $\varepsilon = 0.7$ ($\frac{L}{D} = 1.75$) and $\varepsilon = 0.8$ ($\frac{L}{D} = 2$), flow patterns corresponding to $\varepsilon = 0.9$ ($\frac{L}{D} = 3$) shows narrower wake and formation of elongated vortices from the surface of the downstream rod. This is also observed in some numerical studies (e.g. [51]), which reported narrow wake and broad von Karman vortex streets appearing in the wakes upstream rod at the large spacing ratio for the cases of $\frac{L}{D} = 5$ at $Re = 1.3 \times 10^4$. At this porosity, $\varepsilon = 0.9$ ($\frac{L}{D} = 3$), the patterns of velocity and vorticity along the upper and lower sides of the wake tend to become relatively symmetrical. This observation is in agreement with the 2D PIV characterization of the flow patterns around the rods in a tandem arrangement by Lin *et al.* [5] in the reported case of $\frac{L}{D} = 5.1$ although at $Re = 10^4$. They also reported the variation of time-averaged characteristics of the wake region related to the aforementioned changes in Karman-like vortex shedding.

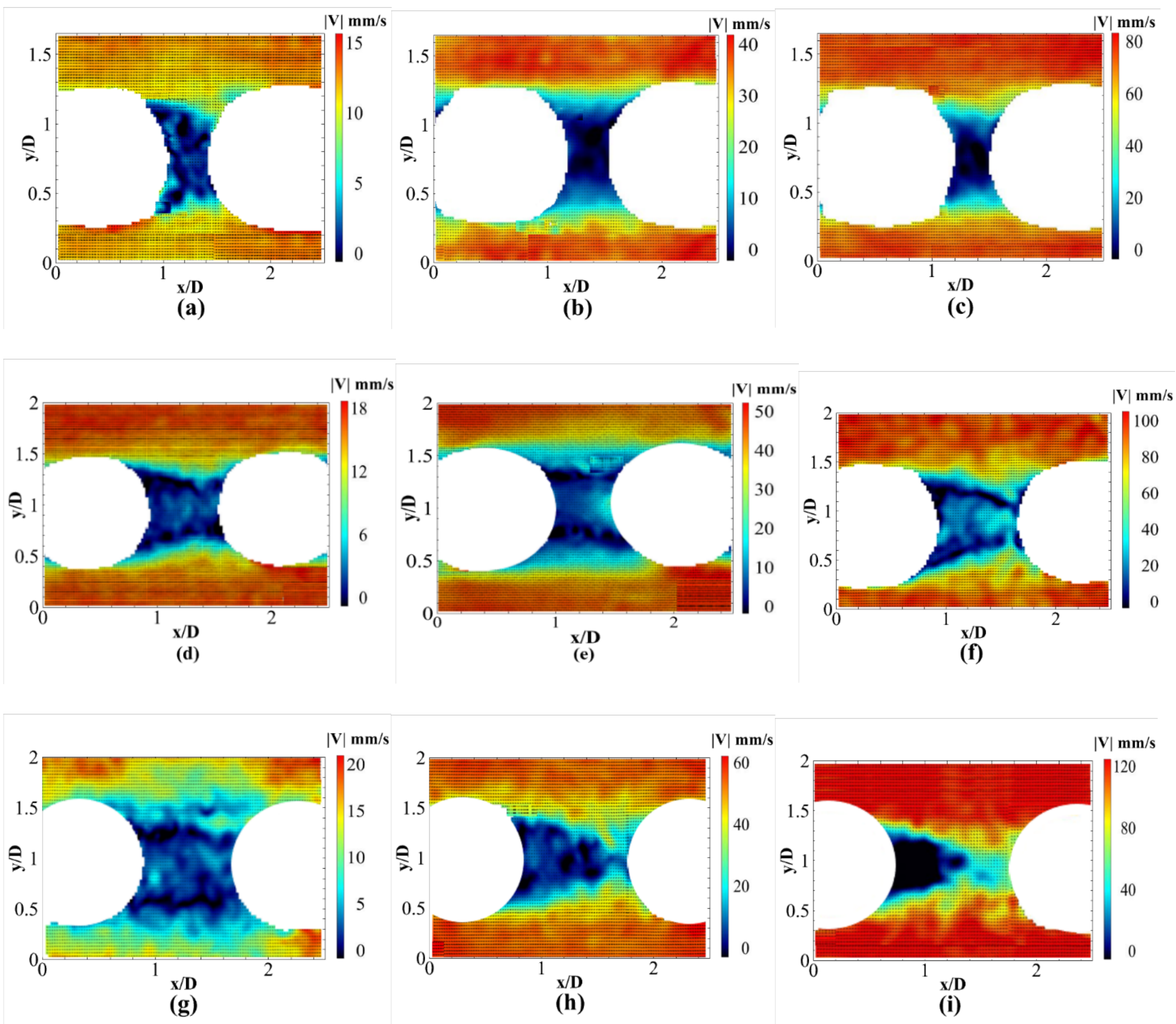

FIG. 10. Time-averaged field of velocity magnitude obtained from the Eulerian bin-averaging of particle trajectories: a) *Re*= 111, b) *Re*= 444, c) *Re*= 890 represent the patterns for $\varepsilon = 0.7$ ($\frac{L}{D} = 1.75$), d) *Re*= 111, e) *Re*= 444, f) *Re*= 890 represent the patterns for $\varepsilon = 0.8$ ($\frac{L}{D} = 2$), and g) *Re*= 111, h) *Re*= 444 , i) *Re*= 890 represent the patterns for $\varepsilon = 0.9$ ($\frac{L}{D} = 3$).

Figure 9 shows the results of the time-averaged out of plane vorticity distribution in the gap region between the rods for $\varepsilon = 0.7$ ($\frac{L}{D} = 1.75$), and $\varepsilon = 0.8$ ($\frac{L}{D} = 2$) at Re =111, 444, and 890. By increasing the Reynolds number, the regions between the rods break up into vortices of different scales where a horseshoe vortex is developed around the rods. The influence of the porosity (or the spacing ratio ($\frac{L}{D}$)) on the stability of the laminar flow is clearly visible along the generated shear layers and the horseshoe vortices. It is also clear that the magnitude of vorticity increases at the higher Reynolds numbers. In all shear layer separation regions, unsteadiness generates waviness leading to the growing evolution of vortices.

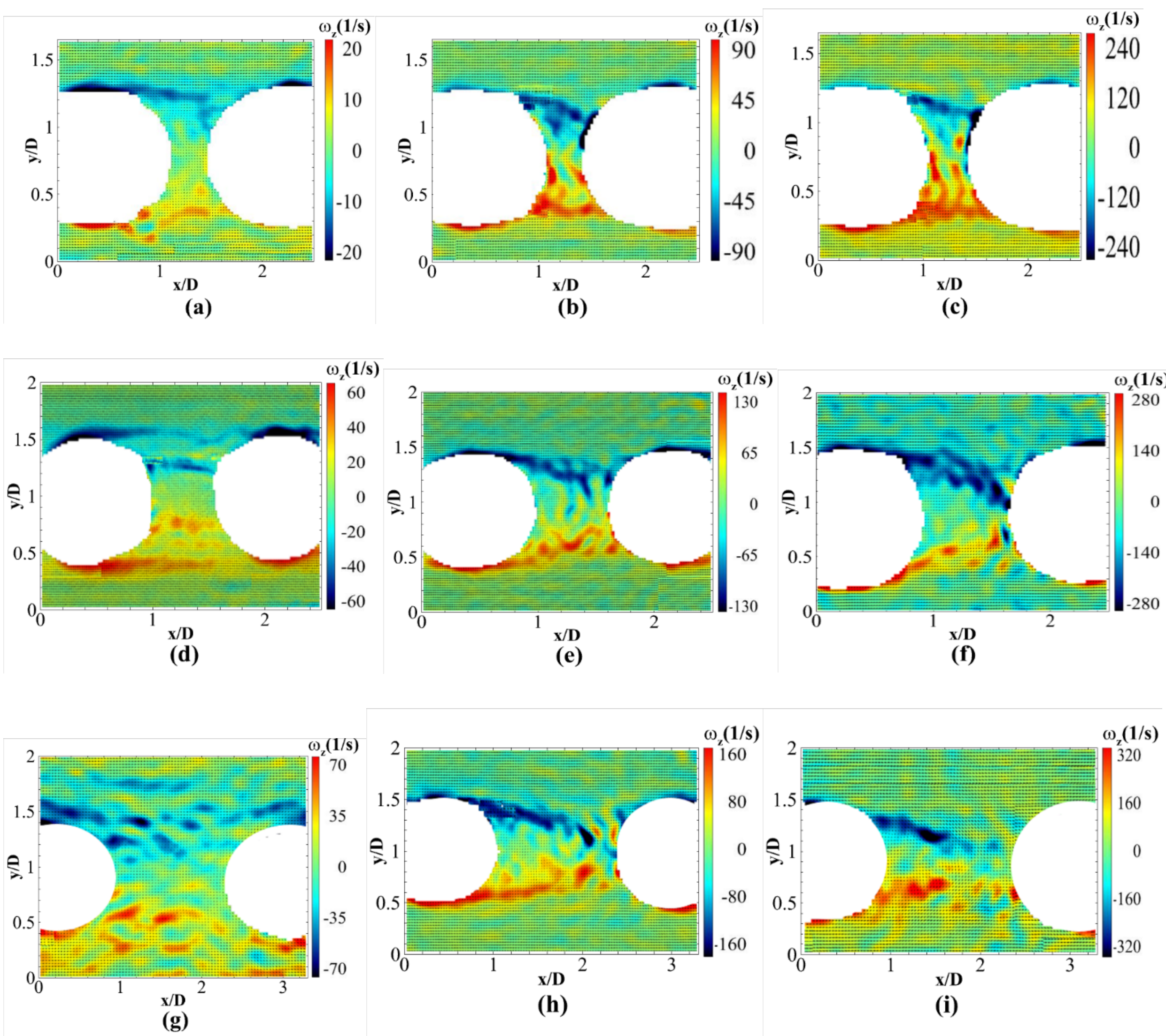

FIG. 11. Time-averaged out of plane vorticity results calculated from the 2D velocity field obtained from the Eulerian binning conversion of particle trajectories. a) *Re*= 111, b) *Re*= 444, c) *Re*= 890 represent the patterns for $\varepsilon = 0.7$ ($\frac{L}{D} = 1.75$), d) *Re*= 111, e) *Re*= 444, f) *Re*= 890 represent the patterns for $\varepsilon = 0.8$ ($\frac{L}{D} = 2$), and g) *Re*= 111, h) *Re*= 444 , i) *Re*= 890 represent the patterns for $\varepsilon = 0.9$ ($\frac{L}{D} = 3$).

As it can be seen in Fig. 9(b, c), for the porous layer with porosity of $\varepsilon = 0.7$ ($\frac{L}{D} = 1.75$), the recirculation regions occurring in the gap region observed to be quasi-stationary, compared to $\varepsilon = 0.8$ ($\frac{L}{D} = 2$). For the higher Reynolds numbers, the shear layer dynamics are very random compared to the lower Reynolds numbers, which exhibits a constant pattern whose mark was also seen in the streak lines in Fig. 6. As can be seen in Fig. 9 (h, i) layers of positive and negative vorticity are getting to the regions close to the surfaces of the downstream rod, which are associated with the unsteady collision of Karman-like vortices. Also, the vorticity patterns become narrower, which is associated with inclined streamlines exterior to this region, as it will be discussed further. With increasing Reynolds number, the flow region between the rods changes considering that the momentum of the incoming flow varies, while at the same time, the dynamics of the transitional and unsteady flow structures along the shear layers are changing. At higher flow velocities, this leads to higher accelerations at the rod's walls and consequently to an increase of the flow separation domain size between the rods. A similar observation has been reported for the flow around a cube in the study by Schröder *et al.* [50] although for a higher Reynolds number.

In order to further quantitatively characterize the flow parameters, Figures 10, 11, and 12 produced to show the distribution of fully averaged streamwise U_x, spanwise U_y, and magnitude of the velocity profiles, calculated as $|V| = \sqrt{{U_x}^2 + {U_y}^2}$, along the centerline in the gap region between the rods based on the spacing ratio of $\frac{L}{D}$ in a porous media models with porosity of a) $\varepsilon = 0.7$ ($\frac{L}{D} = 1.75$), b) $\varepsilon = 0.8$ ($\frac{L}{D} = 2$), and c) $\varepsilon = 0.9$ ($\frac{L}{D} = 3$). It should be mentioned that the time-averaged velocity distribution was also spatially averaged through the depth of measurement, which was physically 2 mm in this experimental study and reported as fully averaged data in the following figures. As observed in Fig. 10, the streamwise velocity shows a positive magnitude all over the centerline region when Re=111. Then, with increasing the Reynolds number to Re=444, and 890, respectively, the mean streamwise velocity (U_x) indicates a negative value until the zero-value occurs. The trends of streamwise velocity profiles agree with the data reported in other studies (e. g., [5,52,53,54]), although the Reynolds number is higher in order of (10^4) in their works. A more portion of the area between the rods shows negative streamwise velocities for the higher Reynolds number of Re=444, and Re=890 indicating the influence of the generation of vortices induced in between the rods. Furthermore, the location of the zero-value streamwise velocity, which is also interpreted as the length of recirculation regions behind the upstream rod is slightly moving with the Reynolds number variation. In fact, with increasing Reynolds number, the zero-value shifts back and becomes closer to the upstream rod. This can be correlated to the transitional flow shear layer separations within the gap region also reported in the study by Hu *et al.* [52] where the flows around two tandem circular rods in the subcritical and supercritical flow regimes are studied through three-dimensional numerical simulations. The spanwise velocity in Fig. 11 (a, b, c), demonstrates negative values in most portion of the gap region (behind the upstream rod), and the absolute values of spanwise velocity drop below 10% of the streamwise velocity but still indicate a net flow across the centerline which is in agreement with the findings in previous works [55, 56]. It can be seen for both streamwise, and spanwise velocity profiles that an increase in the porosity leads to increase in the magnitude of U_x and U_y in the gap region. This is also in agreement with a recent numerical work reported by Maryami *et al.* [57], which presents an experimental study on the unsteady pressure loading for two circular rods in a tandem arrangement for the Reynolds number in the subcritical regime. They reported the velocity profiles in the gap region between the rods, indicating the growth in the magnitude of U_x and U_y with increasing the $(\frac{L}{D})$ ratio.

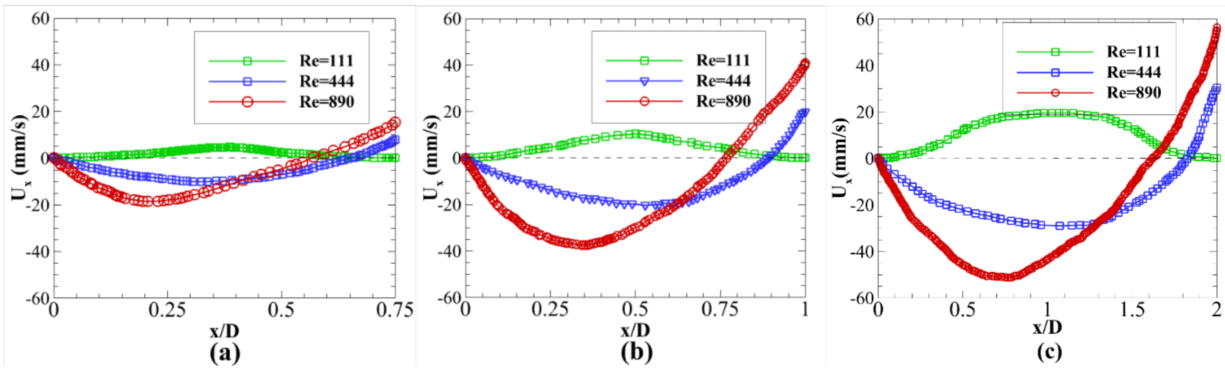

FIG. 12. Distribution of fully averaged streamwise velocity profiles U_x along the centerline in the gap region between the rods based on the spacing ration of $\frac{L}{D}$ in a porous media layer with porosity of a) $\varepsilon = 0.7$ $(\frac{L}{D} = 1.75)$, b) $\varepsilon = 0.8$ $(\frac{L}{D} = 2)$, and c) $\varepsilon = 0.9$ $(\frac{L}{D} = 3)$. (*Re*=111 (green), *Re*=444 (blue), *Re*=890 (Red))

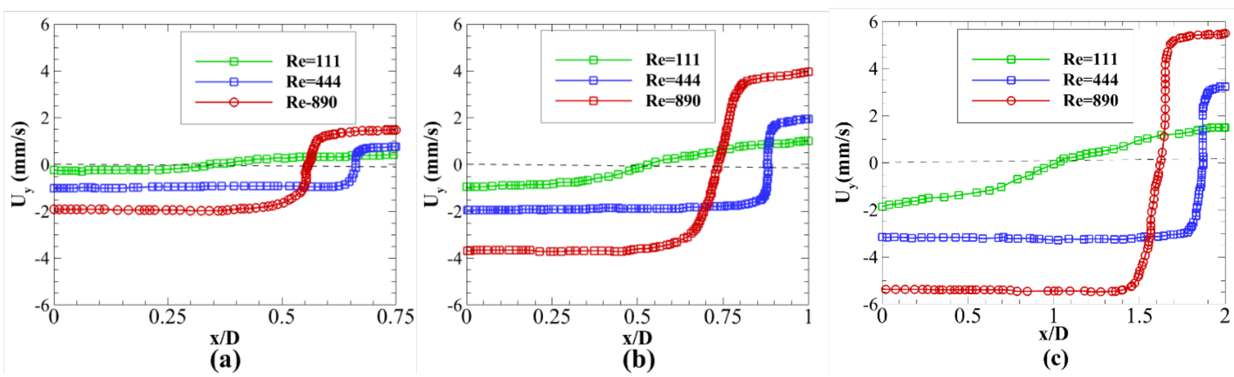

FIG. 13. Distribution of fully averaged spanwise velocity profiles U_y along the centerline in the gap region between the rods based on the spacing ration of $\frac{L}{D}$ in a porous media layer with porosity of a) $\varepsilon = 0.7$ $(\frac{L}{D} = 1.75)$, b) $\varepsilon = 0.8$ $(\frac{L}{D} = 2)$, and c) $\varepsilon = 0.9$ $\left(\frac{L}{D} = 3\right)$. (*Re*=111 (green), *Re*=444 (blue), *Re*=890 (Red))

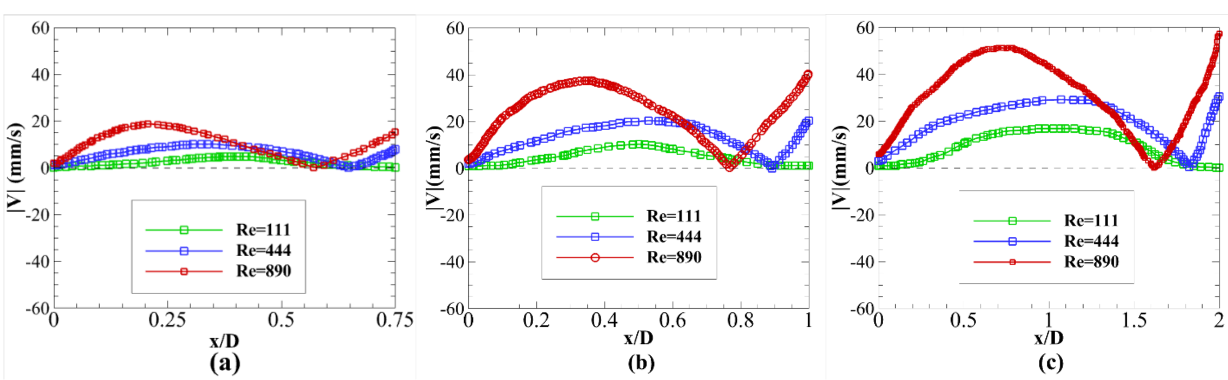

FIG. 14. Distribution of fully averaged magnitude of velocity profiles |V| along the centerline in the gap region between the rods based on the spacing ration of $\frac{L}{D}$ in a porous media layer with porosity of a) $\varepsilon = 0.7$ ($\frac{L}{D} = 1.75$), b) $\varepsilon = 0.8$ ($\frac{L}{D} = 2$), and c) $\varepsilon = 0.9$ ($\frac{L}{D} = 3$). (*Re*=111 (green), *Re*=444 (blue), *Re*=890 (Red)).

In comparison to the existing studies on the examination of flow between two tandem arrangements, this research has been unique in considering the effect of three dimensionality on the flow. The STB volumetric measurements were performed for the first time for such a flow field to provide highly resolved spatial and temporal 3D velocity maps for the targeted measurement volume. In general, we observed both symmetrical and asymmetrical patterns of structures and recirculation regions between the rods depending on the Reynolds number and spacing ratio. Increasing the Reynolds number resulted in less symmetrical patterns of flow structures with respect to the gap centerline, while the spacing ratio affected the symmetry degree randomly. Increasing the Reynolds number resulted in less symmetrical patterns of flow structures with respect to the gap centerline, while the spacing ratio affected the symmetry degree randomly. Increasing porosity lead to significant vortex shedding behind the upstream rod at *Re*=444 and *Re*=890. As the Reynolds number increases, the reattachment point moves backward. These reattachment positions shift slightly along the centerline of the gap region for higher porosity, resulting in an enlarged vortex formation length at the front of the upstream rod. A 2D PIV experiment conducted by Sumner, Price *et al.* [4], revealed a pair of equal strength opposing eddies in the recirculation zone behind each rod. This is while our observation shows that the recirculation regions vary in shape and strength, perhaps because we performed our experiments at a lower Reynolds number compared to their study. Their vorticity data also showed the development of shear layers alongside the rods in the near-wake region, which is relatively similar to what was observed in our vorticity fields shown in Fig. 9. Our observation of Karman-like vortices formed between the rods when the gap region is sufficiently large, was also reported by Lin *et al.*[5], although at a higher Reynolds number. The shear layer separations and the unsteady interaction of the vortices observed in Fig. 9 (e, f, h, i) are in agreement with the data reported by Neuhart et *al.*[8], where they used PIV technique to examine the flow between two tandem rods at $Re = 1.66 \times 10^5$. Performing the experiment at a higher Reynolds number range is one of the future works we aim to do using higher capacity laboratory equipment. In addition, we plan to perform further experiments to examine the larger spacing ratio between the rods ($\frac{L}{D} > 3$) to investigate the distance between the rods where the flow behavior becomes independent, and the downstream rod has increasingly less impact on the development of the gap recirculation zone. We also observed that the flow patterns exhibit some time-dependent states when the Reynolds number increases while this matter requires further future experiments using optical measurement devices capable of a longer record duration for the examined higher flow rates.

IV. Conclusion

Herein, we report an experimental approach to characterize the flow behavior of a Newtonian fluid (DI water) flowing over and through different 3D porous structures using the novel 3D Lagrangian particle tracking velocimetry Shake-the-box (STB) technique. Considering the essential role of the porous structures in both environmental and engineering applications, we aimed to extend the knowledge of flow behavior in steady and unsteady flow regimes using three various porous media models with the porosity of $\varepsilon = 0.7,\ 0.8,$ and 0.9 corresponding to the spacing ratio of $\frac{L}{D} = 1.75, 2, 3$. We specifically focused on examining the flow through two tandem rods inside the porous structures and characterized the flow dynamics features such as 3D velocity trajectories, time-averaged 2D velocity, and vorticity fields in the gap between the rod pairs for three different Reynolds numbers. Increasing Reynolds number significantly affected the symmetry of the flow structures and recirculation region observed in the gap region between the rods. This resulted to the breakage of the gap region into two areas of positive and negative time-averaged streamwise velocity at the centerline. Increasing porosity of the porous media led to a higher instantaneous and averaged magnitude of velocity of the flow trajectories. This research can provide insightful directions for future studies of flows in applications where porous media is present. Furthermore, the investigation of 3D flows of different kinds, such as non-Newtonian fluids and fluids with particles, could be the target of future research avenues using the presented technique.

Acknowledgements

This work has been supported partially by National Science Foundation award #1854376 and partially by Army Research Office award #W911NF-18-1-0356.

References

1. M. Zdravkovich, "The effects of interference between circular cylinders in cross flow," Journal of fluids and structures **1**, 239 (1987).
2. T. Igarashi, "Characteristics of the flow around two circular cylinders arranged in tandem: 1st report," Bulletin of JSME **24**, 323 (1981).
3. T. Igarashi, "Characteristics of the flow around two circular cylinders arranged in tandem: 2nd report, unique phenomenon at small spacing," Bulletin of JSME **27**, 2380 (1984).
4. D. Sumner, S. Price, andM. Paidoussis, "Tandem cylinders in impulsively started flow," Journal of Fluids and Structures **13**, 955 (1999).
5. J.-C. Lin, Y. Yang, andD. Rockwell, "Flow past two cylinders in tandem: instantaneous and averaged flow structure," Journal of Fluids and Structures **16**, 1059 (2002).
6. G. Xu, andY. Zhou, "Strouhal numbers in the wake of two inline cylinders," Experiments in Fluids **37**, 248 (2004).
7. Y. Zhou, andM. Yiu, "Flow structure, momentum and heat transport in a two-tandem-cylinder wake," Journal of Fluid Mechanics **548**, 17 (2006).
8. D. Neuhart, L. Jenkins, M. Choudhari, andM. Khorrami, *Measurements of the flowfield interaction between tandem cylinders* (2009).
9. T. Tsutsui, "Experimental study on the instantaneous fluid force acting on two circular cylinders closely arranged in tandem," Journal of wind engineering and industrial aerodynamics **109**, 46 (2012).
10. M. Weinmann, R. Sandberg, andC. Doolan, "Tandem cylinder flow and noise predictions using a hybrid RANS/LES approach," International Journal of Heat and Fluid Flow **50**, 263 (2014).

11. H. Gopalan, andR. Jaiman, "Numerical study of the flow interference between tandem cylinders employing non-linear hybrid URANS–LES methods," Journal of Wind Engineering and Industrial Aerodynamics **142**, 111 (2015).
12. P. Mirbod, Z. Wu, andG. Ahmadi, "Laminar flow drag reduction on soft porous media," Scientific reports **7**, 17263 (2017).
13. D. Schanz, S. Gesemann, andA. Schröder, "Shake-The-Box: Lagrangian particle tracking at high particle image densities," Experiments in fluids **57**, 1 (2016).
14. S. J. Beresh, J. F. Henfling, R. W. Spillers, andS. M. Spitzer, "'Postage-stamp PIV': small velocity fields at 400 kHz for turbulence spectra measurements," Measurement Science and Technology **29**, 034011 (2018).
15. M. Novara, D. Schanz, N. Reuther, C. J. Kähler, andA. Schröder, "Lagrangian 3D particle tracking in high-speed flows: Shake-The-Box for multi-pulse systems," Experiments in fluids **57**, 1 (2016).
16. M. Novara, D. Schanz, R. Geisler, S. Gesemann, C. Voss, andA. Schröder, "Multi-exposed recordings for 3d lagrangian particle tracking with multi-pulse shake-the-box," Experiments in Fluids **60**, 1 (2019).
17. A. Schröder, D. Schanz, D. Michaelis, C. Cierpka, S. Scharnowski, andC. J. Kähler, "Advances of PIV and 4D-PTV" shake-the-box" for turbulent flow analysis–the flow over periodic hills," Flow, Turbulence and Combustion **95**, 193 (2015).
18. S. Tan, A. Salibindla, A. U. M. Masuk, andR. Ni, *An open-source Shake-the-Box method and its performance evaluation* (2019).
19. P. Mirbod, andN. C. Shapley, "Particle migration of suspensions in a pressure-driven flow over and through a porous structure," Journal of Rheology **67**, 417 (2023).
20. A. Tamayol, andM. Bahrami, "Parallel flow through ordered fibers: an analytical approach," Journal of Fluids Engineering **132**, (2010).
21. P. Mirbod, E. A. Haffner, M. Bagheri, andJ. E. Higham, *An experimental approach to analyze aerosol and splatter formation in a dental practice* (2021).
22. M. Bagheri, A. Moradi Bilondi, E. Taheri, A. Anand, M. F. Schatz, andP. Mirbod, "An experimental analysis of flow transitions in a periodically grooved channel," Bulletin of the American Physical Society (2022).
23. P. Mirbod, E. A. Haffner, M. Bagheri, andJ. E. Higham, "Aerosol formation due to a dental procedure: insights leading to the transmission of diseases to the environment," Journal of the Royal Society Interface **18**, 20200967 (2021).
24. G. Batchelor, "A new theory of the instability of a uniform fluidized bed," Journal of Fluid Mechanics **193**, 75 (1988).
25. E. A. Haffner, andP. Mirbod, "Velocity measurements of dilute particulate suspension over and through a porous medium model," Physics of fluids **32**, 083608 (2020).
26. M. Bagheri, andP. Mirbod, "Effect of Porous Media Models on Rheological Properties of Suspensions," Journal of Non-Newtonian Fluid Mechanics 104876 (2022).
27. F. Nieuwstadt, andH. Keller, "Viscous flow past circular cylinders," Computers & Fluids **1**, 59 (1973).
28. C. Williamson, "Three-dimensional wake transition," Journal of Fluid Mechanics **328**, 345 (1996).
29. C. Wiliamson, "Vortex dynamics in the cylinder wake," (1996).
30. T. Leweke, andC. H. Williamson, "Three-dimensional instabilities in wake transition," European Journal of Mechanics-B/Fluids **17**, 571 (1998).

31. P. Coelho, andF. Pinho, "Vortex shedding in cylinder flow of shear-thinning fluids: I. Identification and demarcation of flow regimes," Journal of non-newtonian fluid mechanics **110**, 143 (2003).
32. J. Chakraborty, N. Verma, andR. Chhabra, "Wall effects in flow past a circular cylinder in a plane channel: a numerical study," Chemical Engineering and Processing: Process Intensification **43**, 1529 (2004).
33. A. Melling, "Tracer particles and seeding for particle image velocimetry," Measurement science and technology **8**, 1406 (1997).
34. R. Dring, "Sizing criteria for laser anemometry particles," (1982).
35. B. Wieneke, "PIV uncertainty quantification and beyond," Delft University of Technology, 2017.
36. B. Wieneke, "Volume self-calibration for 3D particle image velocimetry," Experiments in fluids **45**, 549 (2008).
37. C. Kang, andP. Mirbod, "Pressure-driven pipe flow of semi-dilute and dense suspensions over permeable surfaces," Rheologica Acta **60**, 711 (2021).
38. C. Kang, andP. Mirbod, "Porosity effects in laminar fluid flow near permeable surfaces," Physical Review E **100**, 013109 (2019).
39. P. Mirbod, S. Abtahi, A. M. Bilondi, M. E. Rosti, andL. Brandt, "Turbulent channel flow of suspensions of neutrally buoyant particles over porous media," Journal of Fluid Mechanics **954**, A8 (2023).
40. M. Bagheri, andP. Mirbod, *Effect of Permeability on the Rheology of Non-Brownian Suspensions over Porous Media Models* (2021).
41. M. Bagheri, andP. Mirbod, *Shear flow of suspensions over porous media models* (2020).
42. M. Bagheri, C. Kang, andP. Mirbod, *Suspension flows in a pipe covered with permeable surfaces* (2019).
43. M. Bagheri, V. Kumar, andP. Mirbod, *Instability of dilute suspensions over and through riblets* (2022).
44. M. Bruer, J. Bernsdorf, T. Zeiser, andF. Durst, "Accurate computations of the laminar ow past a square cylinder based on two different methods: lattice-Boltzmann and finite-volume," International Journal of Heat and Fluid Flow **21**, 186 (2000).
45. S. Ishigai, E. Nishikawa, K. Nishimura, andK. Cho, "Experimental study on structure of gas flow in tube banks with tube axes normal to flow: Part 1, Karman vortex flow from two tubes at various spacings," Bulletin of JSME **15**, 949 (1972).
46. S.-y. Wang, F.-b. Tian, L.-b. Jia, X.-y. Lu, andX.-z. Yin, "Secondary vortex street in the wake of two tandem circular cylinders at low Reynolds number," Physical Review E **81**, 036305 (2010).
47. R. Adrian, "Dynamic ranges of velocity and spatial resolution of particle image velocimetry," Measurement Science and Technology **8**, 1393 (1997).
48. D. Schanz, A. Schröder, andS. Gesemann, *Shake the box—a 4D PTV algorithm: accurate and ghostless reconstruction of Lagrangian tracks in densely seeded flows* (2014).
49. S. Tan, A. Salibindla, A. U. M. Masuk, andR. Ni, "Introducing OpenLPT: new method of removing ghost particles and high-concentration particle shadow tracking," Experiments in Fluids **61**, 1 (2020).
50. A. Schröder, C. Willert, D. Schanz, R. Geisler, T. Jahn, Q. Gallas, andB. Leclaire, "The flow around a surface mounted cube: a characterization by time-resolved PIV, 3D Shake-The-Box and LBM simulation," Experiments in Fluids **61**, 1 (2020).

51. M. Abrahamsen Prsic, M. C. Ong, B. Pettersen, andD. Myrhaug, "Large Eddy simulations of flow around tandem circular cylinders in the vicinity of a plane wall," Journal of Marine Science and Technology **24**, 338 (2019).
52. X. Hu, X. Zhang, andY. You, "On the flow around two circular cylinders in tandem arrangement at high Reynolds numbers," Ocean Engineering **189**, 106301 (2019).
53. D. Lockard, *Summary of the tandem cylinder solutions from the benchmark problems for airframe noise computations-I workshop* (2011).
54. R. B. H. Kalvig, M. A. Prsic, andB. Pettersen, *Numerical investigation of 3D flow around two tandem cylinders* (OnePetro, 2016).
55. L. Jenkins, M. Khorrami, M. Choudhari, andC. McGinley, *Characterization of unsteady flow structures around tandem cylinders for component interaction studies in airframe noise* (2005).
56. M. R. Khorrami, M. M. Choudhari, D. P. Lockard, L. N. Jenkins, andC. B. McGinley, "Unsteady flowfield around tandem cylinders as prototype component interaction in airframe noise," AIAA journal **45**, 1930 (2007).
57. R. Maryami, S. A. S. Ali, M. Azarpeyvand, A. A. Dehghan, andA. Afshari, "The influence of cylinders in tandem arrangement on unsteady aerodynamic loads," Experimental Thermal and Fluid Science **139**, 110709 (2022).